Technical Article

On the Effects of Constitutive Properties and Roughness of a Hard Inclusion in Soft Tissue on B-mode Images

Pranav M. Karve[1] [iD]**, Ravindra Duddu[1], Jaime Tierney[2],
Kazuyuki Dei[2]** [iD]**, Ryan Hsi[3], and Brett Byram[2]**

Abstract
We perform finite element modeling of pulse-echo ultrasound of a hard inclusion in a soft tissue to gain a better understanding of B-mode image brightness characteristics. We simulate a pressure wave emitted by an ultrasound transducer through the inclusion-tissue medium by prescribing suitable boundary conditions, and collect the scattered wave response to simulate the behavior of the transducer array used for pulse-echo ultrasound. We form B-mode images from simulated channel data using standard delay and sum beamforming. We establish the accuracy of the finite element model by comparing the point spread function with that obtained from Field II ultrasound simulation program. We also demonstrate qualitative validation by comparing the brightness characteristics of rough and smooth surfaced circular inclusions with experimental images of a cylindrical metal tool immersed in a water tank. We next conduct simulation studies to evaluate changes in B-mode image brightness intensity and contrast related to different constitutive properties, namely, compressibility of the inclusion, impedance contrast between the host and inclusion, and surface roughness of the inclusion. We find that the intensity observed behind a hard inclusion in the axial direction is strongly affected by the compressibility and roughness of the inclusion. Also, the perceived width of the stone based on the intensity is greater for rougher stones. Our study indicates that imaging of compressible inclusions may benefit from targeted B-mode image forming algorithms. Our modeling framework can potentially be useful in differentiating hard inclusions from surrounding parenchyma, and for classifying kidney stones or gallstones.

Keywords
finite element modeling, B-mode ultrasound, elastic wave propagation, reverberation, wave mode conversion

Introduction

Ultrasound imaging is widely utilized in medical diagnostics because it is inexpensive, accessible, portable, and avoids ionizing radiation exposure. In fact, ultrasound is the preferred imaging modality for kidney stone or gallstone diagnosis[1] and is gaining popularity as a real-time imaging technique for guided interventional procedures.[2] However, ultrasound is known to suffer from poor performance (e.g., reduced sensitivity and specificity) compared with computed tomography (CT) when imaging kidney stones in soft tissue.[1,3–7] Although B-mode ultrasound imaging of soft tissues is susceptible to image degradation from a variety of mechanisms,[8,9] the imaging of hard inclusions is uniquely challenged by the large constitutive property mismatch with soft tissue and inclusion roughness. For example, high-impedance

mismatches can cause multi-path scattering or reverberation leading to the appearance of comet-tail and ring-down artifacts or shadowing. Because certain artifacts (e.g., a kidney stone shadow or tail) are used

[1]Department of Civil and Environmental Engineering, Vanderbilt University, Nashville, TN, USA
[2]Department of Biomedical Engineering, Vanderbilt University, Nashville, TN, USA
[3]Department of Urologic Surgery, Vanderbilt University Medical Center, Nashville, TN, USA

Corresponding author:
Ravindra Duddu, Department of Civil and Environmental Engineering, Vanderbilt University, 2301 Vanderbilt Place, Nashville, TN 37240-0002, USA.
Email: ravindra.duddu@Vanderbilt.Edu

clinically for detection and classification, better understanding of the physics behind artifact appearance through computer simulation can potentially lead to improved diagnostic performance (e.g., improved sensitivity, specificity, and stone sizing). Furthermore, a comprehensive understanding of ultrasonic wave interactions at the inclusion–tissue interface can aid the development of improved imaging algorithms, including advanced beamforming methods that could enable artifact-free imaging. To this end, we perform finite element modeling to simulate ultrasonic wave propagation in a soft-tissue medium containing a hard inclusion to better understand the effects of constitutive properties and inclusion roughness on wave propagation and B-mode image brightness characteristics.

The presence and origin of imaging artifacts when imaging hard inclusions (e.g., stones or mineral crystals) or metallic objects have been widely reported in clinical settings, and investigated using in vitro and in vivo studies.[2,10–20] The physics behind artifact appearance in specific clinical scenarios can be broadly identified based on the fundamentals of linear acoustics (i.e., sound propagation) in inhomogeneous media.[21] Despite extensive observations, relatively few studies in the literature have investigated the physics of wave scattering in the inclusion–tissue environment in the context of imaging. Earlier studies employed experimental and analytical modeling techniques to understand acoustic wave scattering by metallic cylinders and spheres immersed in water.[22–27] However, such analytical studies would only provide a limited understanding of the wave scattering by stones, which are often characterized by the rough surface texture of crystalline mineral deposits (e.g., calcium oxalate[28] or cystine).[29] Therefore, this limits the utility of analytical studies in development of improved algorithms for stone imaging. With the availability of robust numerical simulation tools developed in the recent decades, it is now possible to conduct detailed computational modeling studies of the stone–tissue imaging problem and overcome the limitations of analytical studies.

Many simulation tools, Field II,[30,31] FOCUS,[32] finite-difference-time-domain (FDTD) simulators,[33,34] are available for modeling wave scattering in heterogeneous, lossy acoustic media. Because it is reasonable to approximate an incompressible viscoelastic soft tissue as an acoustic material medium,[35,36] these existing simulation tools have been extremely useful in the context of soft-tissue imaging. However, the same acoustic media approximations may not be appropriate for hard inclusions embedded in soft tissues that exhibit high impedance contrast and different constitutive behavior. It is well understood that stones and metallic objects are

better described using compressible linear elastic material models (i.e., Poisson's ratio $\nu < 0.5$), rather than a linear acoustic or incompressible viscoelastic material model used to describe soft tissues. A consequence of this constitutive behavior mismatch is that we need to simulate the propagation and scattering of two types of body waves—a faster pressure wave and a slower shear wave—including wave mode conversion at oblique inclusion–tissue interfaces. Therefore, we employ a suite of compressible and nearly incompressible elastic/viscoelastic constitutive models for the hard inclusion and soft tissue to investigate wave propagation and scattering using the finite element method (FEM). The advantage of the FEM is that it is well developed to handle incompressible elastic and viscoelastic material models, and describe complex inclusion geometries,[37] but the disadvantage is that it is computationally more expensive than semi-analytical simulation tools such as FIELD II or FOCUS.

In this study, we employ the FEM because it allows us to study wave propagation in elastic media, including pressure (longitudinal) and shear (transverse) waves, and investigate wave scattering in relation to material (constitutive) and geometric parameters. The propagation of wave energy within the inclusion and the nature of the reflected waves sensed by the transducer differ for the case of acoustic, nearly incompressible elastic and compressible elastic materials because of wave mode conversion. Previously, the inadequacy of acoustic material model for a kidney stone embedded in soft tissue has been established in the context of lithotripsy.[38–41] However, the implications of material models and surface roughness on image brightness and contrast in B-mode ultrasound imaging have not been previously investigated. While it is understood that reverberation artifacts are manifested when pressure waves reflect multiple times before returning back to the ultrasound transducer, the role of shear waves and wave mode conversion has not been studied. To the best of our knowledge, there exist no similar simulation studies analyzing imaging artifacts in the ultrasound literature. The outcome of our study highlights the unique challenges for imaging compressible media (calcification in breast, testicle, vascular environments) and implies that these scenarios may benefit from targeted image formation algorithms. The rest of this article is organized as follows: in the section "Model Formulation," we describe the material models, surface roughness models, and the governing equations of the wave mechanics for stone–tissue environments; in the "Method" section, we discuss the computational and experimental methods that describe the set up of numerical and laboratory experiments. In the "Results and Discussion" section, we present the results from our

numerical simulations performed using the commercial software Abaqus in two dimensions including model verification and validation studies; finally, in the "Conclusion" section, we provide a summary of this study along with some concluding remarks.

Model Formulation

Domain Setup

Figure 1 shows the schematic sketch of the two-dimensional (2D) domain under plane strain conditions used for describing the constitutive model equations. Specifically, we use acoustic, incompressible elastic, and viscoelastic material models to describe the constitutive behavior of the homogeneous host medium, and acoustic, incompressible elastic, and compressible elastic material models to describe the constitutive behavior of the inclusion. We model the excitation induced by the ultrasonic transducer in the host medium by imposing suitable Dirichlet conditions on the boundary of the domain. We chose the dimensions of the computational domain (D_1 and D_2) to be large enough so that the waves reflected from the domain edges do not interfere
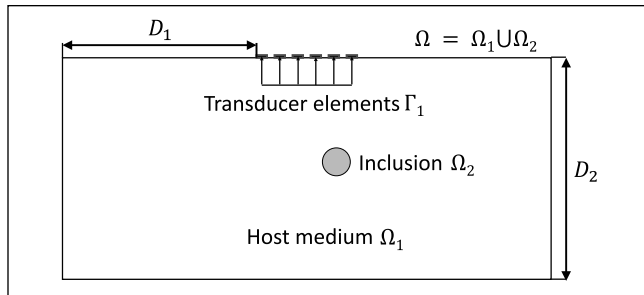

Figure 1. Schematic of the computational domain consisting of a homogeneous host (tissue) and an embedded inclusion (stone). $D_1 \approx 0.041$ m and $D_2 \approx 0.060$ m is used in our simulations.

with the signals recorded by the transducer elements for imaging. In all cases, we use silent initial conditions everywhere in the computational domain.

Acoustic–acoustic Model

This constitutive model is suited to study wave scattering due to impedance mismatch in an acoustic host containing an acoustic inclusion. The pertinent governing equations are given by,

$$K_f \mathbf{V} \cdot (\nabla p) = \rho_f \ddot{p}, \quad \text{for } \mathbf{x} \in \Omega_1 \cup \Omega_2 \quad (1)$$

$$p = p_{\text{trans}}(t), \quad \text{for } \mathbf{x} \in \Gamma_1 \quad (2)$$

where $p \equiv p(\mathbf{x}, t)$ is the acoustic pressure, ρ_f is the density, and K_f is the bulk modulus of the acoustic medium. The pressure time history $p_{\text{trans}}(t)$ is prescribed at the face of transducer elements (see Figure 2). In the above equations (and henceforth), an over dot (˙) implies the partial derivative with respect to time, $()^T$ denotes transpose, $\mathbf{I}$ is the identity tensor, and the spatio-temporal dependence of variables has been suppressed in the governing equations for brevity. Table 1 gives the material properties pertinent to this model used in our simulations. The values of K_f and ρ_f for the host medium and the inclusion are chosen to match the longitudinal wave speeds ($C_p = \sqrt{K_f/\rho_f}$) obtained experimentally in those media.

Elastic–acoustic Model

This constitutive model is suited to study wave scattering in a nearly incompressible elastic tissue containing a compressible or nearly incompressible elastic inclusion. Thus, this model captures both pressure and shear wave propagation inside the stone, as well as in the tissue.
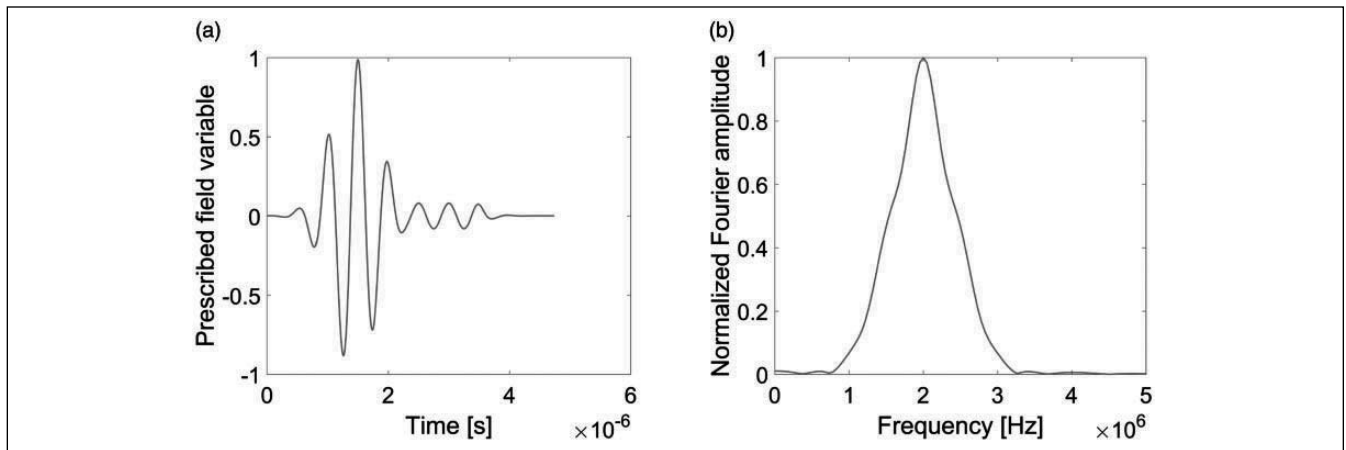

Figure 2. Time signal used for modeling transducer actuation: (a) Time signal for the prescribed field variable. (b) Normalized Fourier transform of the time signal.

The governing equations for the elastic wave propagation are given by,

$$\mathbf{V} \cdot \sigma = \rho_s \ddot{\mathbf{u}}, \quad \text{for } \mathbf{x} \in \Omega_1 \cup \Omega_2 \tag{3}$$

$$\sigma = \mu_s \left[\mathbf{V}\mathbf{u} + \mathbf{V}\mathbf{u}^T - \frac{2}{3}(\mathbf{V} \cdot \mathbf{u})\mathbf{I} \right] + K_s(\mathbf{V} \cdot \mathbf{u})\mathbf{I} \tag{4}$$

$$\dot{\mathbf{u}} = \dot{\mathbf{u}}_{\text{trans}}(t), \quad \text{for } \mathbf{x} \in \Gamma_1 \tag{5}$$

where $\sigma \equiv \sigma(\mathbf{x}, t)$ is the Cauchy stress, $\mathbf{u} \equiv \mathbf{u}(\mathbf{x}, t)$ is the solid displacement; ρ_s is the density, μ_s is the shear modulus, and K_s is the bulk modulus for the elastic medium. The velocity time history $\dot{\mathbf{u}}_{\text{trans}}(t)$ is prescribed at the face of transducer elements (see Figure 2). Table 2 gives the material property values pertinent to this model used in our numerical simulations. We remark that an elastic material model with a very small shear modulus ($\mu_s \to 0$, or Poisson's ratio $\nu \to 0.5$) can be used to simulate the wave propagation in acoustic media. This elastic material exhibits almost no compressibility, so henceforth we refer to this material as incompressible (instead of *nearly incompressible*) for brevity. We use mechanical properties of renal calculi measured and reported by Zhong et al.[42] We choose three stone types: struvite or magnesium ammonium phosphate hexahydrate (MAPH), uric acid (UA), and calcium oxalate monohydrate (COM) with varying (longitudinal wave) impedance for our numerical experimentation.

Table 1. Material Properties for the Case of an Acoustic Host and Acoustic Inclusion.

Domain	K_f Pa	ρ_f kg/m^3	C_p m/s
Host medium (Ω_1)	2.37×10^9	1000	1538
Inclusion (Ω_2)	12.4×10^9	1585	2795
Point-like target (Ω_2)	37.2×10^9	1585	4844

Elastic–elastic Model.

Viscoelastic–elastic Model

This constitutive model is suited to study wave scattering in a incompressible viscoelastic tissue containing a compressible elastic inclusion. Thus, this model captures time-dependent pressure wave attenuation inside the tissue, in addition to the pressure and shear wave propagation inside the stone. The governing equations for the inclusion and the Dirichlet boundary condition remain same as that for the elastic–elastic model (Equations (3)-(5)). To describe the volumetric constitutive behavior of the incompressible viscoelastic host, we adopt a one-element generalized Maxwell model, wherein it is assumed that the volumetric stress (i.e., pressure) is strain rate dependent, but the deviatoric stress is not. Thus, in this model, the pressure waves in the viscoelastic tissue medium experience attenuation, but we assume the shear waves do not experience attenuation. Because the scattering of pressure waves due to the compressible elastic stone is of primary importance in the present investigation of imaging algorithms, this assumption is reasonable. The governing equations for the viscoelastic medium are given by

$$\mathbf{V} \cdot \sigma = \rho_s \ddot{\mathbf{u}}, \quad \text{for } \mathbf{x} \in \Omega_2, \tag{6}$$

$$\sigma = \sigma_{\text{dev}} - p\mathbf{I}, \tag{7}$$

$$\sigma_{\text{dev}} = \mu_s [(\mathbf{V}\mathbf{u} + \mathbf{V}\mathbf{u}^T) - \frac{2}{3}(\mathbf{V} \cdot \mathbf{u})\mathbf{I}], \tag{8}$$

$$p \equiv p(\mathbf{x}, t) = -K_s \int_0^t k_R(t - s)\dot{\epsilon}_{\text{vol}}(\mathbf{x}, s)\mathrm{d}s, \tag{9}$$

$$\epsilon_{\text{vol}}(\mathbf{x}, t) = \mathbf{V} \cdot \mathbf{u}(\mathbf{x}, t), \tag{10}$$

where σ_{dev} is the deviatoric stress tensor, p is the volumetric stress, K_s is the instantaneous bulk modulus, $k_R(t)$ is the dimensionless bulk relaxation modulus,

Table 2. Material Properties for the Case of a Incompressible Elastic Host Containing an Incompressible/Compressible Elastic Inclusion.

Domain	Compressibility	K_s Pa	μ_s Pa	ρ_s kg/m^3	C_p m/s	C_s m/s
Host medium (Ω_1)	Incompressible	2.37×10^9	1.67×10^3	1000	1538	1.3
MAPH (Ω_2)	Compressible	6.74×10^9	4.24×10^9	1585	2795	1635
MAPH (Ω_2)	Incompressible	1.23×10^{10}	8.68×10^3	1585	2795	2.3
UA (Ω_2)	Compressible	1.42×10^{10}	3.31×10^9	1546	3471	1464
UA (Ω_2)	Incompressible	1.86×10^{10}	13.30×10^3	1546	3471	2.9
COM (Ω_2)	Compressible	2.96×10^{10}	9.26×10^9	2038	4535	2132
COM (Ω_2)	Incompressible	4.19×10^{10}	29.94×10^3	2038	4535	3.8
Point-like target (Ω_2)	Compressible	2.02×10^{10}	12.70×10^9	1585	4844	2833

Note that we refer to a nearly incompressible elastic material as incompressible for brevity. MAPH = magnesium ammonium phosphate hexahydrate; UA = uric acid; COM = calcium oxalate monohydrate.

and ϵ_{vol} is the volumetric strain. For the one-element generalized Maxwell model, we define the dimensionless relaxation modulus using a Prony series expression with two constants, k_1 and τ_1, as

$$k_R(t) = 1 - k_1\left(1 - e^{-\frac{t}{\tau_1}}\right) \qquad (11)$$

The Prony series parameters (k_1, τ_1) govern the wave attenuation and dispersive nature of the viscoelastic medium. Typically, a linear attenuation model is used to simulate ultrasonic wave attenuation in tissues, with an attenuation coefficient $\alpha_p \approx 0.7\,\mathrm{dB/cm/MHz} \approx 8.05\,\mathrm{Np/m/MHz}$.[43] In this work, we chose the Prony series parameters such that the attenuation variation in our viscoelastic model mimics the attenuation variation defined by the coefficient $\alpha_p \approx 0.7\,\mathrm{dB/cm/MHz}$. Using graphical calibration, we arrived at the values of $k_1 = 0.0085$ and $\tau_1 = 0.052\,\mu s$. Figure 3 shows the variation in attenuation in the frequency range of interest (i.e., 0.5-3 MHz). Table 3 gives the material property values pertinent to this model that were used in our numerical simulations. Note that a viscoelastic medium is dispersive in nature, so the wave speeds depend on the frequency. Table 3 gives wave speeds at a frequency of 2 MHz.

Surface Roughness

For simplicity, we describe the surface roughness of the inclusion by introducing a periodically rough boundary defining the perimeter of the inclusion, as shown in Figure 4. The parameters that describe the roughness are (a) the radius of the inner circle, R_{in}; (b) the radius
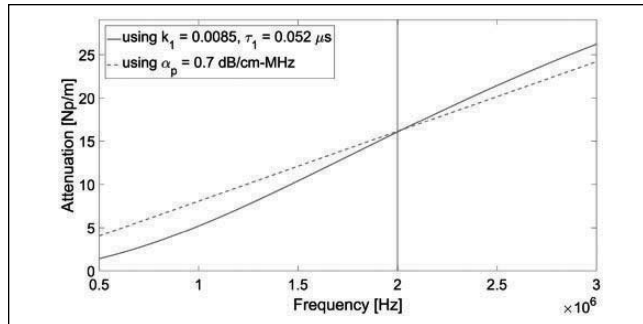

Figure 3. Variation in attenuation coefficient with frequency for the generalized Maxwell viscoelastic model.

of the outer circle, R_{out}; and (c) the number of peaks or valleys along the outer perimeter of the inclusion, n_{peaks}. The parameter that quantifies the roughness of the inclusion depending on the probing wavelength can be defined as

$$r = \frac{R_{out} - R_{in}}{\lambda} \qquad (12)$$

where $\lambda = C_p/f$ is the probing wavelength, C_p is the longitudinal wave speed, and f is the center frequency of ultrasonic excitation. We remark that the relationship between the roughness parameter r and the commonly used root mean square (RMS) roughness parameter R_q[44] is given by

$$R_q = \sqrt{R_{out}^2 + \frac{r^2\lambda^2}{3} - r\lambda R_{out}} \qquad (13)$$

Method

Finite Element Simulation

We use the commercial finite element software Abaqus[45] to solve the governing equations presented in the "Model Formulation" section. We use four-noded, bilinear, reduced-integration finite elements with hourglass control (CPE4R).[45] At each time-step, the second time-derivative of the field variable (pressure or displacement) is obtained by solving the discretized system of governing equations. An explicit time integration (central difference) scheme is used to compute the value of the field variable at each finite element node. The time-step size is automatically chosen by Abaqus so as to satisfy the Courant–Friedrichs–Lewy (CFL) condition. We ensure that the element size $h \leq \lambda/15$ where λ is the wavelength of the center frequency of the broadband pulse transmitted by each element.

Simulation Data Acquisition

In an ultrasound imaging system, the ultrasonic transducer acts as a wave source as well as the wave receiver.

Table 3. Material Properties for the Case of a Incompressible Viscoelastic Host Containing a Compressible Elastic Inclusion.

Domain	K_s Pa	μ_s Pa	ρ_s kg/m^3	C_p m/s	C_s m/s
Host medium (Ω_1)	2.37×10^9	1.67×10^3	1000	1538	1.3
MAPH (Ω_2) (compressible)	6.74×10^9	4.24×10^9	1585	2795	1635
UA (Ω_2) (compressible)	1.42×10^{10}	3.31×10^9	1546	3471	1464
COM (Ω_2) (compressible)	2.96×10^{10}	9.26×10^9	2038	4535	2132

MAPH = magnesium ammonium phosphate hexahydrate; UA = uric acid; COM = calcium oxalate monohydrate.
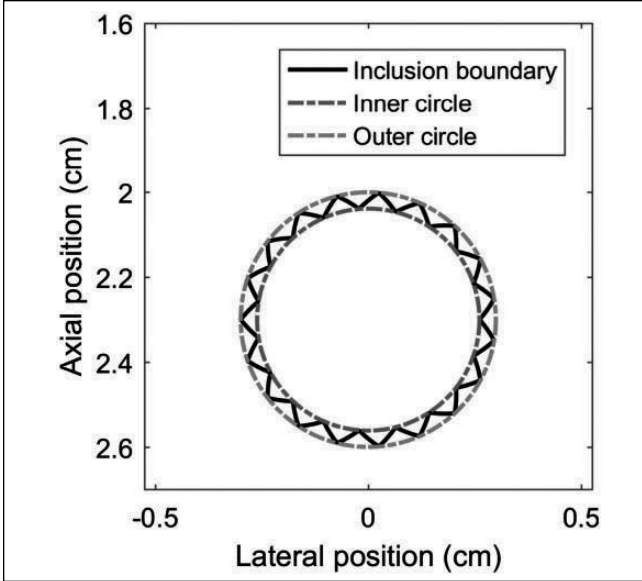
Figure 4. A generic rough inclusion, $R_{in} = 0.0026$ m, $R_{out} = 0.003$ m, and $n_{peaks} = 19$.

In the source mode, the piezoelectric elements in the transducer receive a time varying electric signal and vibrate to generate an ultrasonic pulse in the imaged media. In classical acoustics, transducer element directivity refers to the amplification/cancelation of wave motion in the excited medium due to constructive/destructive interference of waves radiated by different parts of a single, vibrating transducer element. In our simulations, each transducer element is approximated using few discrete finite elements. In the transmit mode, the finite element's nodes (i.e., vertices) vibrate and the total wavefield, which is the result of superposition of the waves emitted by all nodes constituting the element, is computed at all points in the domain of interest. This process is performed for all transducer elements. In the receive mode, we record the vibrations of individual nodes and sum them to obtain the resulting vibrations of the element. Thus, the channel data are created using the superposition of vibrations of individual vibrating parts for the transducer element. Thus, the finite element simulation process includes a discretized version of the classical acoustic directivity. In the receiver mode, scattered waves impart vibrations to each of the piezoelectric elements and the motion of a piezoelectric element generates an electric signal. These spatially and temporally sampled signals are often referred to as ultrasound channel data. The channel data are acquired by ultrasound systems and then beamformed to obtain the ultrasonic image. Note that the face of a piezoelectric element is in contact with the domain being imaged, and vibrations experienced by the face due to the scattered waves can be assumed to be the aggregate effect of the

wave motion on the face. Therefore, in our finite element simulations, we record the time history of field quantities (i.e., pressure or velocity) at the finite element nodes located below transducer element faces to collect the response during the ultrasound imaging process. We find the average of the response (pressure or velocity time history) recorded at multiple finite element nodes below a given face of the transducer element to arrive at the channel data-record for that transducer element. We process the channel data to develop a B-mode image using delay and sum beamforming. Specifically, we use a plane wave that insonifies a large segment of the media, and then we use parallel receive beamforming to make a complete image from a single plane wave transmit event.

Imaging Algorithm

In order to obtain the B-mode image using parallel receive beamforming, we first record the time history of field quantities (i.e., pressure or velocity) at the finite element nodes located below transducer element faces to collect the response during the ultrasound imaging process. We then sum the response (pressure or velocity time history) recorded at multiple finite element nodes below a given face of the transducer element to arrive at the channel data-record for that transducer element. The known sound speed for the simulations is then used to delay the channel data, which is then summed using conventional methods. The B-mode image intensity along the channel can be computed as $BM_i(z)$, for $z \in (0, z_{max})$, $i = 1, 2, \ldots, n_{chan}$, where n_{chan} denotes the number of transducer elements (channels), the z-axis is along the axial direction, and $z_{max} \leq D_2$ is the maximum imaging depth that depends on the total duration of data acquisition and C_p^{bmode}. We report the power of the BM_i (envelope) data defined as

$$P_i(z) = 20 \log_{10}\left(\frac{BM_i(z)}{BM^{ref}}\right), \quad \text{for } z \in (0, z_{max}), \quad (14)$$
$$i = 1, 2, \ldots, n_{chan},$$

where BM^{ref} is the maximum value of the envelope, and $P_i(z)$ is the power along the ith channel in decibels (dB). All B-mode images in this article show brightness on a 60 dB scale. Similarly, the variation of power in the lateral direction, for a given depth (z_*) is computed using

$$P_k(z_*) = 20 \log_{10}\left(\frac{BM_k(z_*)}{BM_x^{ref}}\right), \quad \text{for } k = 1, 2, \ldots, n_{chan}$$

$$(15)$$

where n_{chan} denotes the number of transducer elements (channels) used, and BM_x^{ref} is the maximum value of the

envelope along $z = z_*$. The variation of the power of the B-mode envelope along the axial direction provides insights about reverberation artifacts, which typically show up as uniformly spaced bright bands. In practice, these artifacts either degrade a B-mode image or can be used for detection of kidney stones (e.g., comet-tail artifact). In either case, a better understanding of the reverberation artifacts can lead to improvements in B-mode imaging. In clinical applications, the size of hard inclusions (kidney stones) embedded in soft tissues is estimated using the *the spread of brightness* in the lateral direction. Thus, study of brightness characteristics along the lateral direction help evaluate the effect of surface roughness on the error in stone size estimation.

Qualitative Verification with Point Spread Function (PSF) Evaluation

To verify our simulation results, a comparison study is performed against a known semi-analytical solution. We compare the PSF generated by the finite-element-based source–receiver system for acoustic and elastic media with the PSF of integral-equation-based source–receiver system for acoustic media generated by Field II.[30,31] Thus, the aim of this study is to establish the capability of our finite-element-method-based simulator to accurately describe wave scattering by a point target or heterogeneity and to correctly model low amplitude pressure wave propagation in otherwise homogeneous media. We remark that Pinton et al. have used similar studies to qualitatively verify their (FDTD) wave physics simulator model.[33]

In the Field II program, the incident pressure at a point heterogeneity (or at any point in the medium) is calculated using the spatial impulse response function.

This function defines the incident pressure at a point in space due to a temporal Dirac delta excitation from a given wave source. The Field II program simulates this point target wave scattering, using an integral-equation-based resolution of the governing physics. In contrast, the FEM uses discretized domains of finite area in 2D (or volume in three-dimensional [3D]), and the governing equations of wave propagation are satisfied in the weak (integral) form. Due to the finiteness of discretization elements, it is not possible to represent a point scatterer unless the mesh size is infinitesimal. Therefore, in our finite element simulations in two dimensions, we model a point-like target (or scatterer) with a relatively small area compared with the characteristic wavelength of the ultrasound wave excitation. The point-like scatterer is located 2 cm below the center of the transducer. We use an element size of 35 μm, and the scatterer is specified by a square-shaped inclusion of size 70 μm. We consider the acoustic–acoustic and elastic–elastic material models discussed in the previous section and the corresponding material properties are given in Tables 1 and 2. The homogeneous host and the target inclusion have a pressure-wave-impedance contrast of about 5. The wave source is a transducer with 64 elements (element width and pitch of 0.245 mm) placed on the top boundary of the 2D domain of interest (see Figure 1). We excite the elements of the transducer with the signal given in Figure 5. We use a zero degree plane wave transmission; meaning, we do not use time delay across the transducer elements on transmit. We also do not use apodization on transmit. We note that in the transmit mode, the 64-element array acts as a line source because there is no apodization and time delay. However, in receive mode, it acts as an array with 64 elements
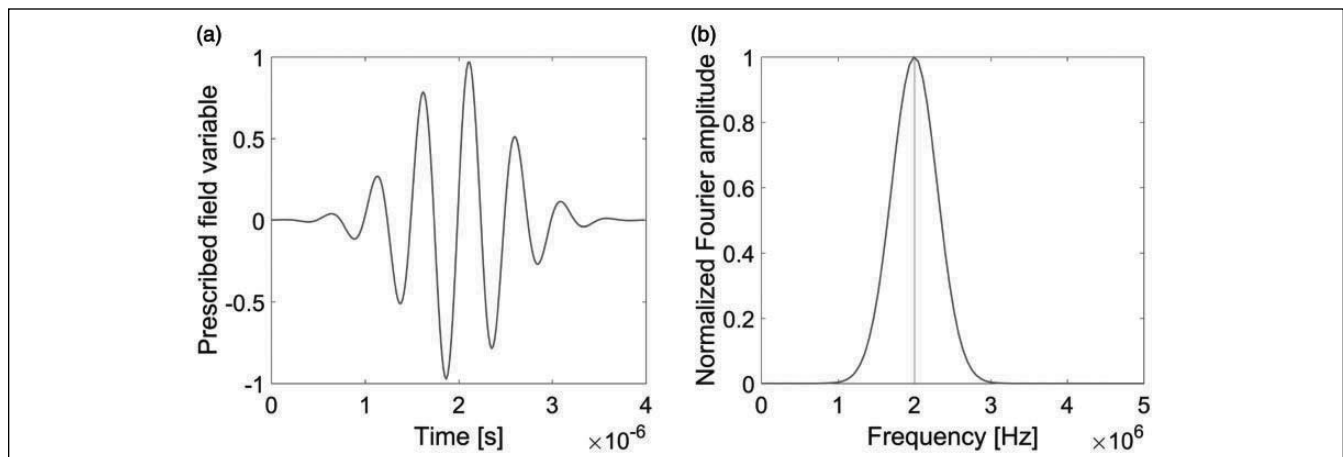

Figure 5. Time signal used for modeling transducer excitation to evaluate the linear model behavior using the point spread function: (a) Time signal for the prescribed field variable. (b) Normalized Fourier transform of the time signal.

because the collected response is delayed and summed to obtain the channel data for each element separately from the corresponding finite element nodes.

Qualitative Validation with Laboratory Experiment

The aim here is to establish the validity of the finite-element-method-based wave mechanics simulator compared with experimentally obtained B-mode images of rough and smooth circular objects. In the laboratory experiment, we immersed a cylindrical, metal-alloy (steel) tool in a degassed water tank and imaged it at approximately 2 cm away the surface of the transducer in the axial direction. The tool's shaft had smooth and rough portions, which were both imaged and compared with the respective smooth and rough circular inclusion simulations. Due to the qualitative nature of the comparison, we did not characterize or establish any metric for the degree of roughness and simply idealized the surface characteristics of the rough tool based on visual examination. The diameter of the cylindrical tool was approximately 6 mm and it had a regular roughness (spiky) pattern on the surface. We used this information to create an idealized geometry for the rough tool in our simulations.

We acquired data using the Verasonics Vantage 128 (Verasonics, Inc., Kirkland, Washington) and the P4-2v ultrasound transducer. Channel data were obtained from a single unsteered plane wave, and B-mode images were made using parallel receive beamforming. The acquisition parameters were matched to the simulation parameters with 64 receive elements, a plane wave transmit, a 2.08 MHz center frequency, and pitch of 0.3 mm. We assumed a sound speed $C_p^{\text{bmode}} = 1480$ m/s for beamforming. We next performed finite element simulations of wave scattering due to smooth and rough circular inclusions embedded in the homogeneous host medium, which represent the metal tool immersed in an incompressible fluid medium. In our 2D finite element simulations, we placed the circular inclusion of 6 mm diameter such that its centroid is situated at an axial distance of 2.3 cm from the center of the transducer. We used alloy-steel-like material properties for the inclusion: $C_p = 5741$ m/s, $\rho_s = 7850$ kg/m^3, $C_s = 3148$ m/s for the compressible inclusion case, and $C_s = 5$ m/s for the incompressible inclusion case. We define the surface roughness of the inclusion using a saw-toothed circular shape, wherein the height of each tooth is chosen as half of the central wavelength (corresponding to the central frequency) in the soft tissue. We use $R_{\text{out}} = 3$ mm, $r = 0.5$ ($R_q \approx 2.8$ mm), and $n_{\text{peaks}} = 19$ to model a circular inclusion with rough surface. We use incompressible and compressible elastic material models for the inclusion.

Simulation Studies

We conducted simulations to evaluate the effect of inclusion compressibility, host–inclusion impedance contrast, and inclusion surface roughness on the brightness characteristics of B-mode images. The material models, transducer specifications, data acquisition methodology, and imaging algorithms remain same as those described in sections "Model Formulation," "Finite Element Simulation," "Simulation Data Acquisition," and "Imaging Algorithm." To demonstrate the effect of compressibility of the elastic inclusion, we computed the divergence (i.e., pressure wave component) and curl (i.e., shear wave component) of the displacement field inside the domain at different times for incompressible and compressible inclusions. In the B-mode imaging algorithm, a (pressure) wave speed (C_p^{bmode}) is typically assumed to synchronize the scattered signals recorded by different transducer elements. A snapshot of the wavefield in the domain of interest at time t_{snp} gets interpreted as brightness in the B-mode image at depth z_{snp}, where

$$z_{\text{snp}} \approx \left(t_{\text{snp}} + \frac{d_{\text{snp}}}{C_p^{\text{bmode}}} \right) \times \frac{C_p^{\text{bmode}}}{2} \qquad (16)$$

and d_{snp} is the depth at which the disturbance traveling toward the transducer lies at $t = t_{\text{snp}}$. To demonstrate the effect of impedance contrast on B-mode imaging of stones, we simulate wave scattering by inclusions of varying impedance. To this end, we use mechanical properties of renal calculi measured and reported by Zhong et al.[42] The material properties used in our finite element simulations are given in Table 2. Impedance and impedance contrast with the background tissue for the three stone types selected for this study are given in Table 4. To demonstrate the effect of stone surface roughness, we compare wave scattering by a rough and smooth circular inclusion. We note that the rough inclusion is a better representation of a real kidney stone embedded in a soft tissue, because stones (or calculi) are calcified mineral deposits usually characterized by rough surfaces.[28,29] We simulate wave scattering by uric-acid-stone-like inclusions (Table 2) with $R_{\text{out}} = 3$ mm, $r = 0$

Table 4. Impedance Contrast for Different Kidney Stones[42] (Based on Host Tissue Impedance of 1.54×10^6 Pa s/m).

Stone Type	Impedance (Pa s/m)	Impedance Contrast with Host Tissue
MAPH	4.43×10^6	2.88
UA	5.37×10^6	3.49
COM	9.24×10^6	6.01

MAPH = magnesium ammonium phosphate hexahydrate; UA = uric acid; COM = calcium oxalate monohydrate.

(smooth surface, $R_q = 3$ mm), and $r = 0.1, 0.5$, and 1 (rough surfaces, $R_q \approx 3$, 2.8, and 2.6 mm, respectively), and report on the power variation along the axial and lateral directions. Thus, we vary either contrast or the roughness (but not both) to evaluate the effect of each factor separately. The effect of impedance contrast is studied for a roughness value $r = 0$, and the effect of roughness is studied for a single impedance-contrast value.

Results and Discussion

In this section, we present and discuss the results from our numerical simulations along with those from Field II and laboratory experiments used for verification and validation.

Qualitative Verification with PSF Evaluation

We simulated wave scattering in a homogeneous medium containing a point scatterer using the linear acoustic simulator Field II and a point-like scatterer using the finite element software Abaqus,[45] as discussed in section "Qualitative Verification with Point Spread Function Evaluation." In the finite element simulations, we use the procedure described in the "Simulation Data Acquisition" section to arrive at the channel data for each transducer element. The B-mode images of the point-like scatterer for the material and transducer parameters given in Tables 1 and 2 are depicted in Figure 6. It is evident from Figure 6 that within the limitations of the domain discretization used to represent a point, the FEM matches well with the integral-equations-based semi-analytical method used by the Field II program. The normalized channel data for one of the channels (Channel 32) are plotted in Figure 7. Note that the PSF scattering in finite element simulations is due to a very small but finite area (a few finite elements), whereas that obtained using Field II considered the analytical expression for a point (infinitesimally small) scatterer. It can be observed in Figure 7 that the channel data for the cases match very well, despite the small difference in the size of the target in these two cases. Thus, this benchmark simulation verifies our finite-element-method-based wave mechanics simulator and provides confidence in the first-order linear behavior. Furthermore, we see that the incompressible elastic host model was able to create a B-mode image similar to that obtained using an acoustic material host model. Therefore, in all subsequent studies, we use the incompressible elastic material model to simulate the behavior of an acoustic host and acoustic inclusion.

Qualitative Validation with Laboratory Experiment

To establish the validity of our finite-element-method-based wave mechanics simulator and to illustrate the effect of surface roughness on brightness in B-mode images, we conducted laboratory experimental studies, as described in the "Qualitative Validation with Laboratory Experiment" section. The experimentally obtained B-mode images along a plane through the middle of the rough and smooth cylindrical tool are shown in Figure 8(a) and (d). The corresponding images obtained by modeling water as an incompressible elastic medium and the cylindrical tool as an incompressible elastic inclusion are shown in Figure 8(b) and (e). The images obtained by modeling the cylindrical tool as a compressible elastic circular inclusion are shown in Figure 8(c) and (f). Only if the inclusion is considered to be a compressible elastic solid, the images obtained from our simulations match well with those obtained from our experiments for rough and smooth circular inclusions.

Simulation Studies

Effect of inclusion compressibility. To study the effect of stone compressibility on B-mode imaging, we compare B-mode images of an acoustic and elastic inclusion with
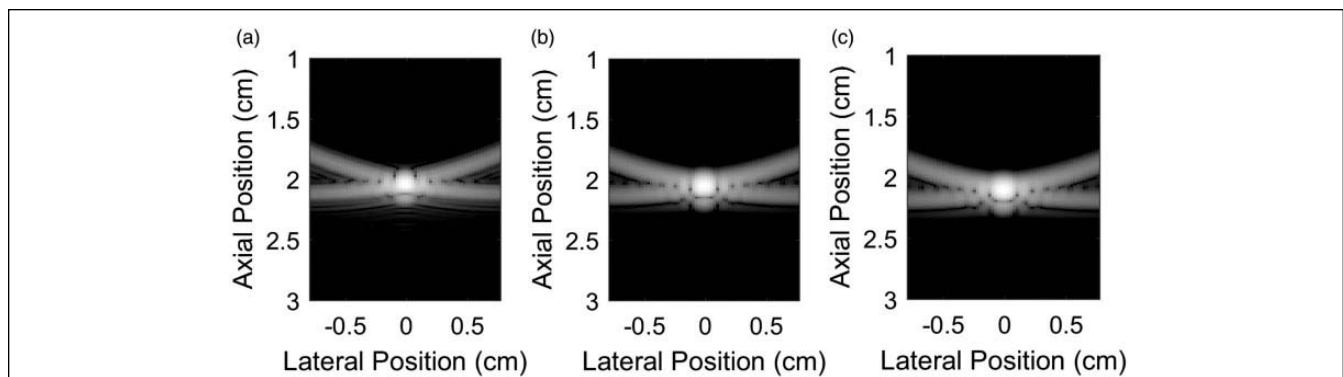

Figure 6. The point spread functions are compared for the (a) acoustic host and acoustic target (Field II),[30,31] (b) acoustic host and acoustic target (Abaqus),[45] and (c) incompressible elastic host and elastic target (Abaqus).[45] The good agreement between these three cases verifies our approach.
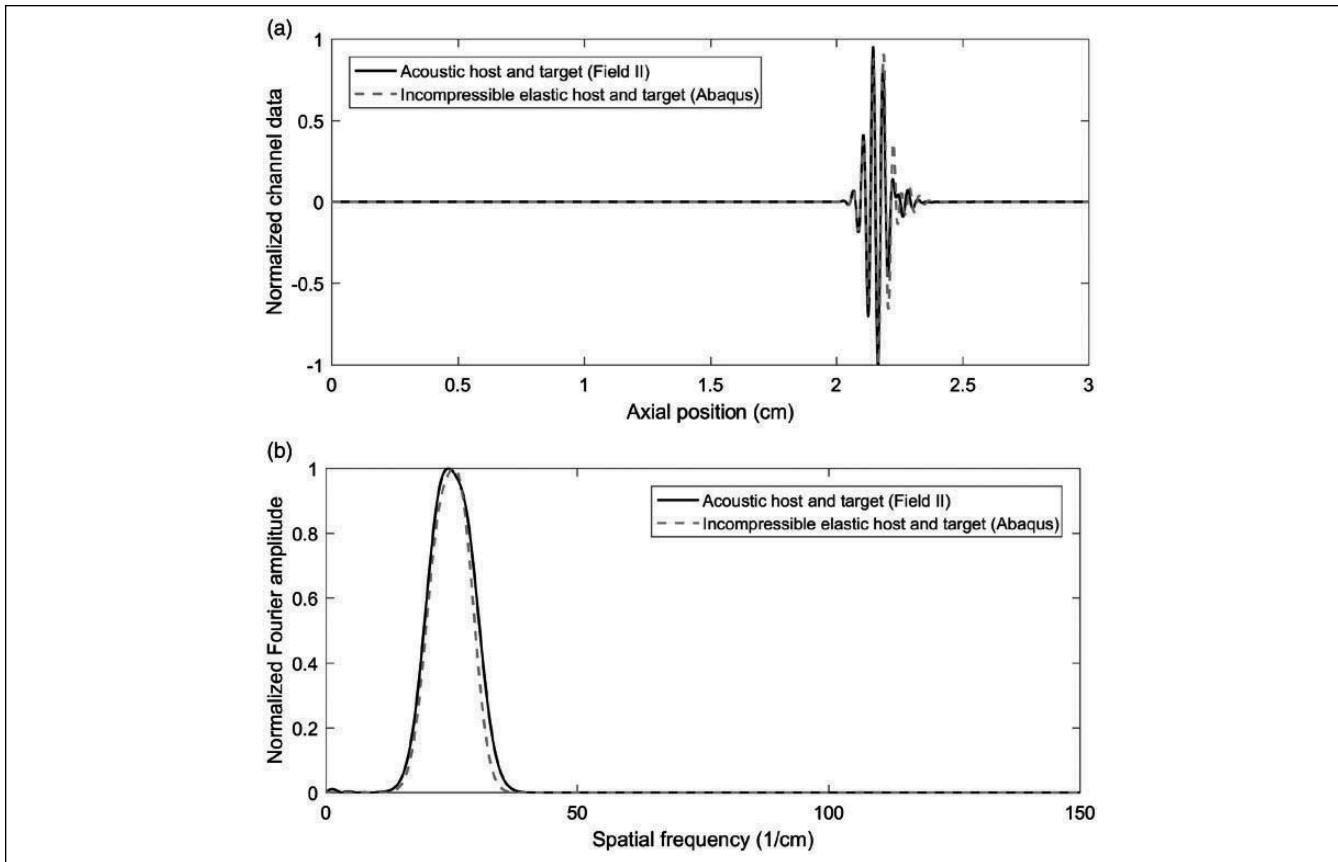
Figure 7. Channel data and Fourier spectrum of channel 32 obtained using Field II and Abaqus[45]: (a) Channel data. (b) Fourier spectrum of the channel data.
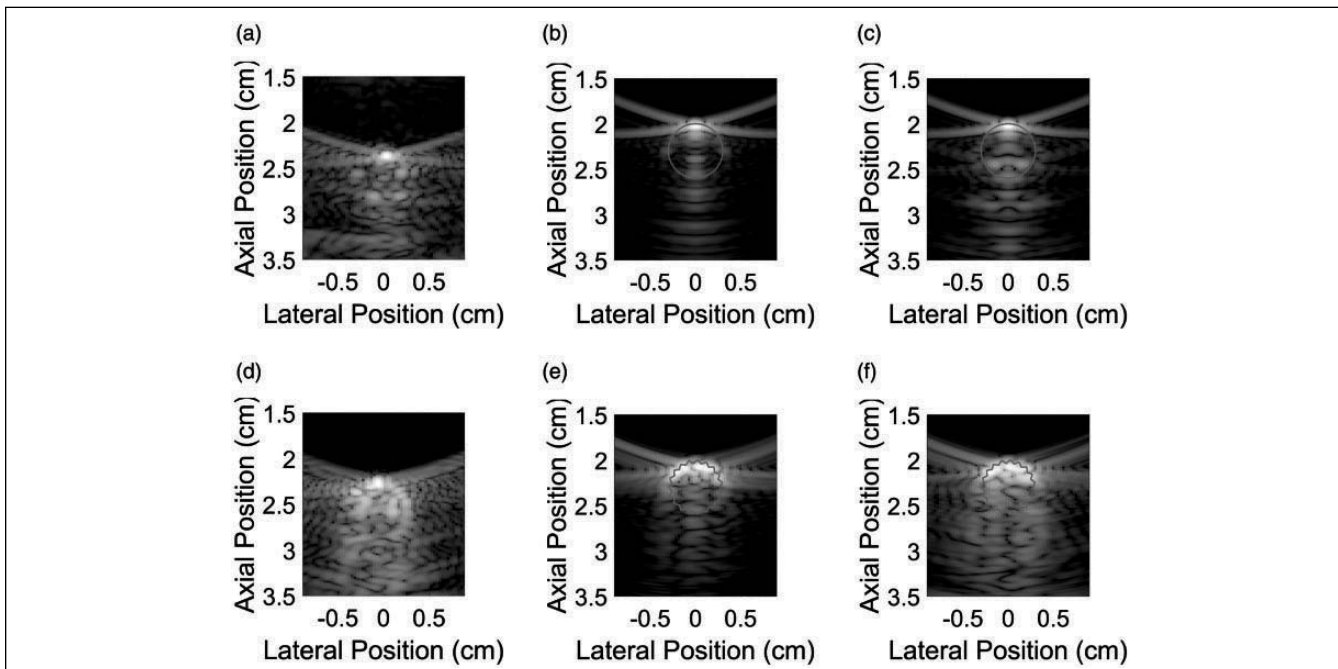

Figure 8. B-mode images for smooth and rough circular inclusions are compared. The images for smooth and rough tool immersed in a water tank are shown in (a) and (d), respectively. Smooth and rough incompressible inclusions are shown in (b) and (e), respectively. Smooth and rough compressible inclusions are shown in (c) and (f), respectively. The images of compressible inclusions match better with the experiments. Also, the rough compressible inclusion creates the most diffused reverberation.

identical impedance contrast and roughness. As an example, we use the material properties of the MAPH stone (Table 2) for all inclusions, and $R_{out} = 3\,mm$, $r = 0.5$, $n_{peaks} = 19$ to model the surface roughness of the rough inclusions. In the first column of Figure 9, we show the B-mode images for the circular inclusion for different material models and surface roughness for the inclusion. The reverberation-induced backscatter, that is, the increase in backscatter signal beyond the leading interface of the inclusion, in the case of compressible inclusions, is much greater than that compared with the case of incompressible elastic inclusions. We took the viscoelastic–elastic model (i.e., incompressible viscoelastic tissue and compressible elastic stone) as the benchmark and evaluated pixel-by-pixel relative error of B-mode image intensity for the acoustic–acoustic, and elastic–elastic models (Table 1). Because we used the same finite element mesh for generating these images,

it is appropriate to evaluate the mean relative error this way. Table 5 gives the pixel-by-pixel relative errors (in %). We find that incompressible elastic model for the tissue and compressible elastic model for the stone has the least mean relative error with the benchmark, which explains the visual match between the corresponding B-mode images in Figure 9.

Owing to the circular shape of the inclusion, most of the wave energy transmitted by the transducer experiences oblique incidence and undergoes mode conversion at the host–inclusion interface in the case of a compressible elastic inclusion. The origin of the increased backscatter in the case of compressible inclusions can be tracked based on the dilatational and equivoluminal components of the wavefield at/near the inclusion. In the second and third columns of Figure 9, we show the divergence (i.e., pressure wave component) and curl (i.e., shear wave component) of the displacement field at $t_{snp} = 28.33\,\mu s$,
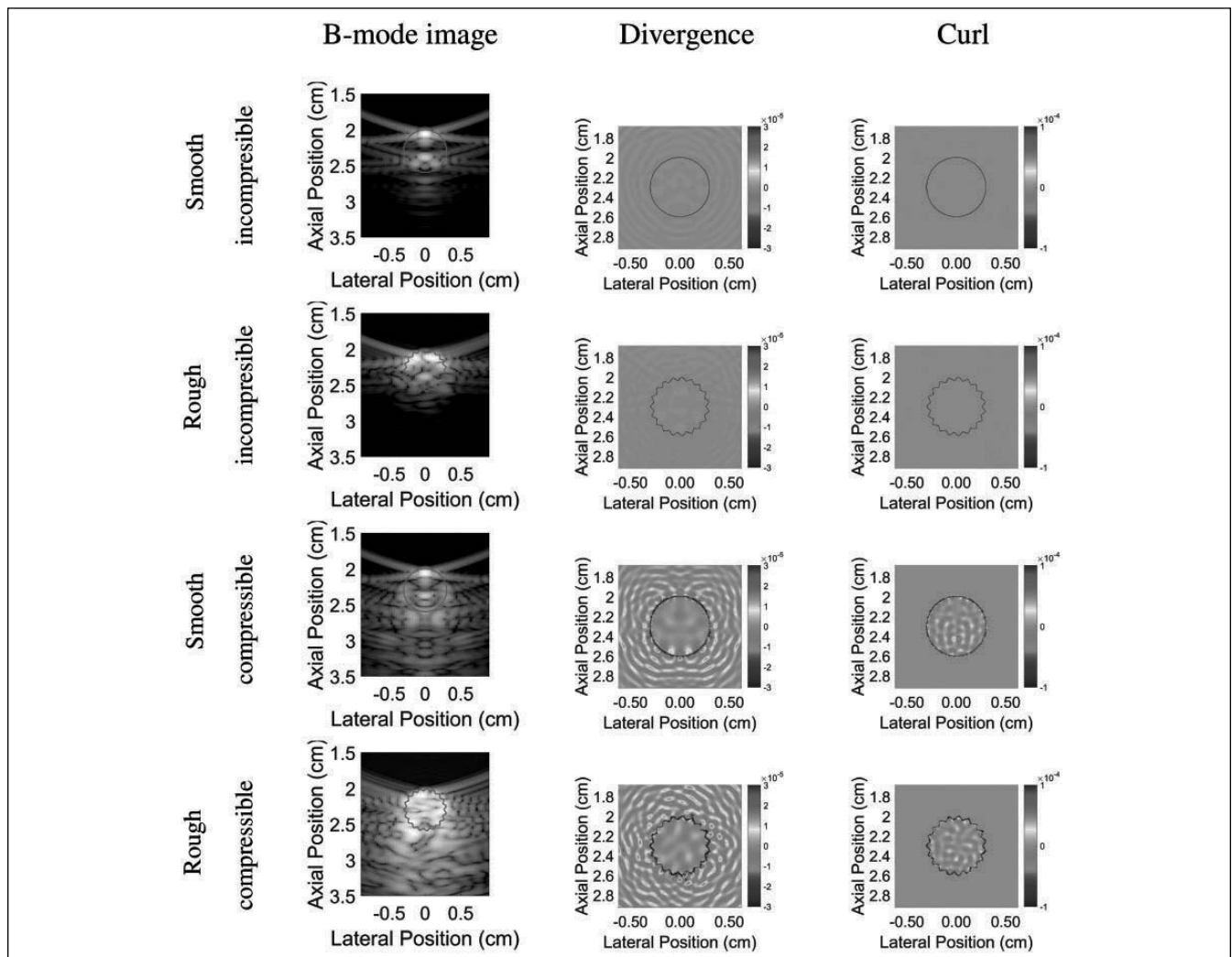

Figure 9. B-mode images of smooth and rough inclusions for various material models are shown. The divergence of displacement (i.e., pressure waves) and the curl of displacement (i.e., transverse waves) at $t_{snp} = 28.33\,\mu s$ (corresponding to $z_{snp} = 3.3\,cm$) are shown. Under the incompressiblity assumption, there are no transverse waves.

Table 5. Pixel-by-pixel Mean Relative Error for Intensity in B-mode Images.

Constitutive Model for the Tissue	Constitutive Model for the Stone	Smooth Stone	Rough Stone
Viscoelastic	Compressible elastic	Benchmark	Benchmark
Elastic	Compressible elastic	5.65%	6.47%
Incompressible elastic	Incompressible elastic	26.65%	47.59%

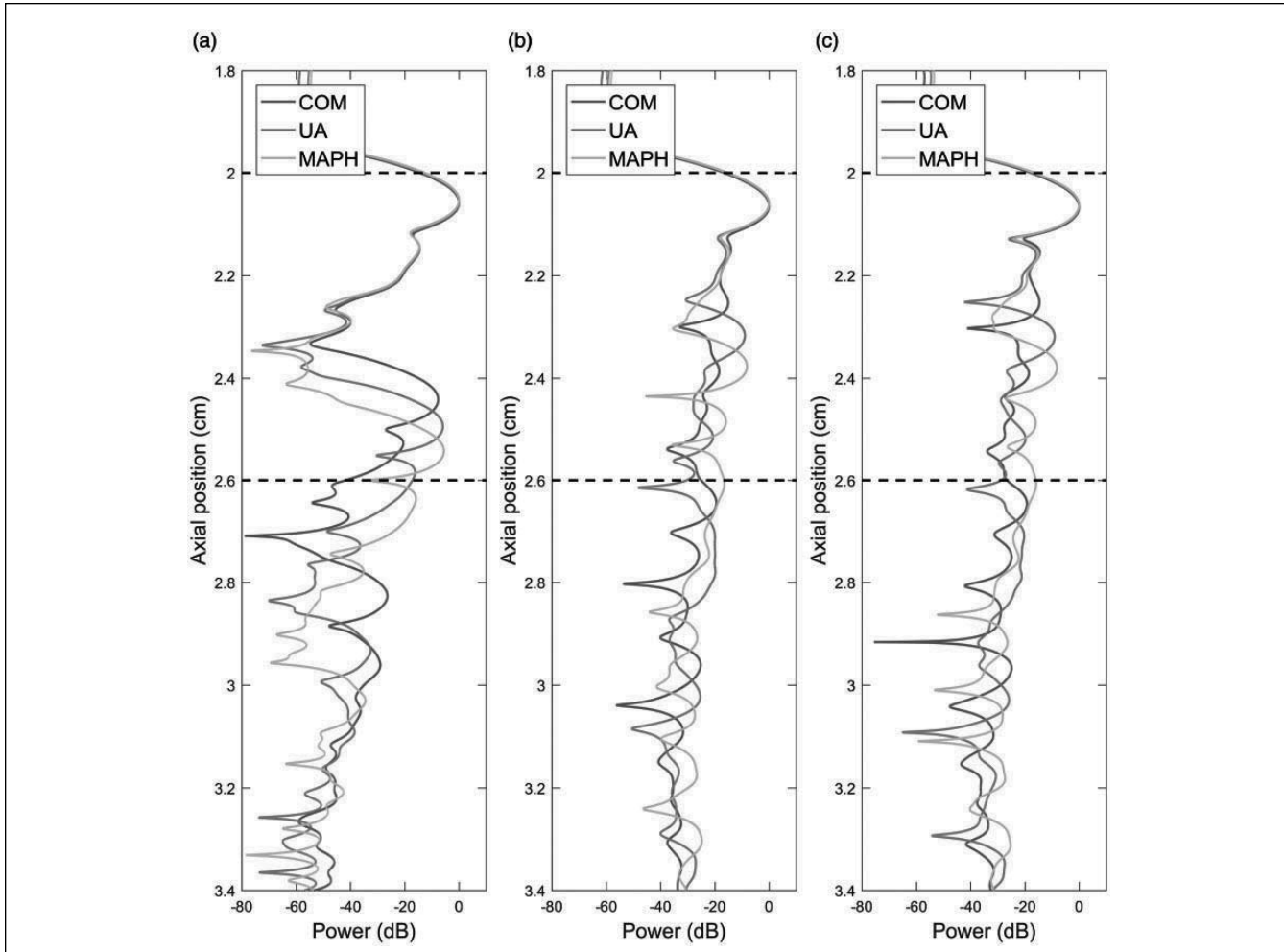The case of viscoelastic tissue with compressible elastic inclusion is taken as the benchmark.

Figure 10. The effect of impedance contrast on B-mode images of smooth, hard inclusions; the variation of power ($P_{32}(z)$ in Equation (14)) through the depth for incompressible and compressible elastic inclusions in incompressible elastic host are shown in (a) and (b), respectively. The variation of power along the depth for compressible elastic inclusion in viscoelastic host is shown in (c). It is notable that the backside of the inclusion is only detectable for incompressible elastic inclusions. Three different types of stones are compared, calcium oxalate (COM), uric acid (UA), and magnesium ammonium phosphate hexahydrate (MAPH). The dashed lines denote the extremities of the inclusion in all plots.

which corresponds to $z_{snp} \approx 3.3$ cm for the value of C_p^{bmode} used to create the B-mode image (1540 m/s). It is apparent that shear waves propagate inside the compressible smooth/rough circular inclusion, and reverberate inside the stone. Each time the reverberating shear waves encounter a stone–tissue boundary, some of the energy in the shear waves is converted into a pressure wave and is transmitted through the tissue. A portion of

the scattered wave energy is recorded by transducer elements and interpreted by the B-mode algorithm as longitudinal waves returning from depth $z_{snp} \approx 3.3$ cm. Similar behavior at other times results in the extended backscatter behind the inclusion. This study suggests that the compressibility of the elastic inclusion magnifies the reverberation-induced backscatter and the spread of brightness behind the inclusion. These reverberation
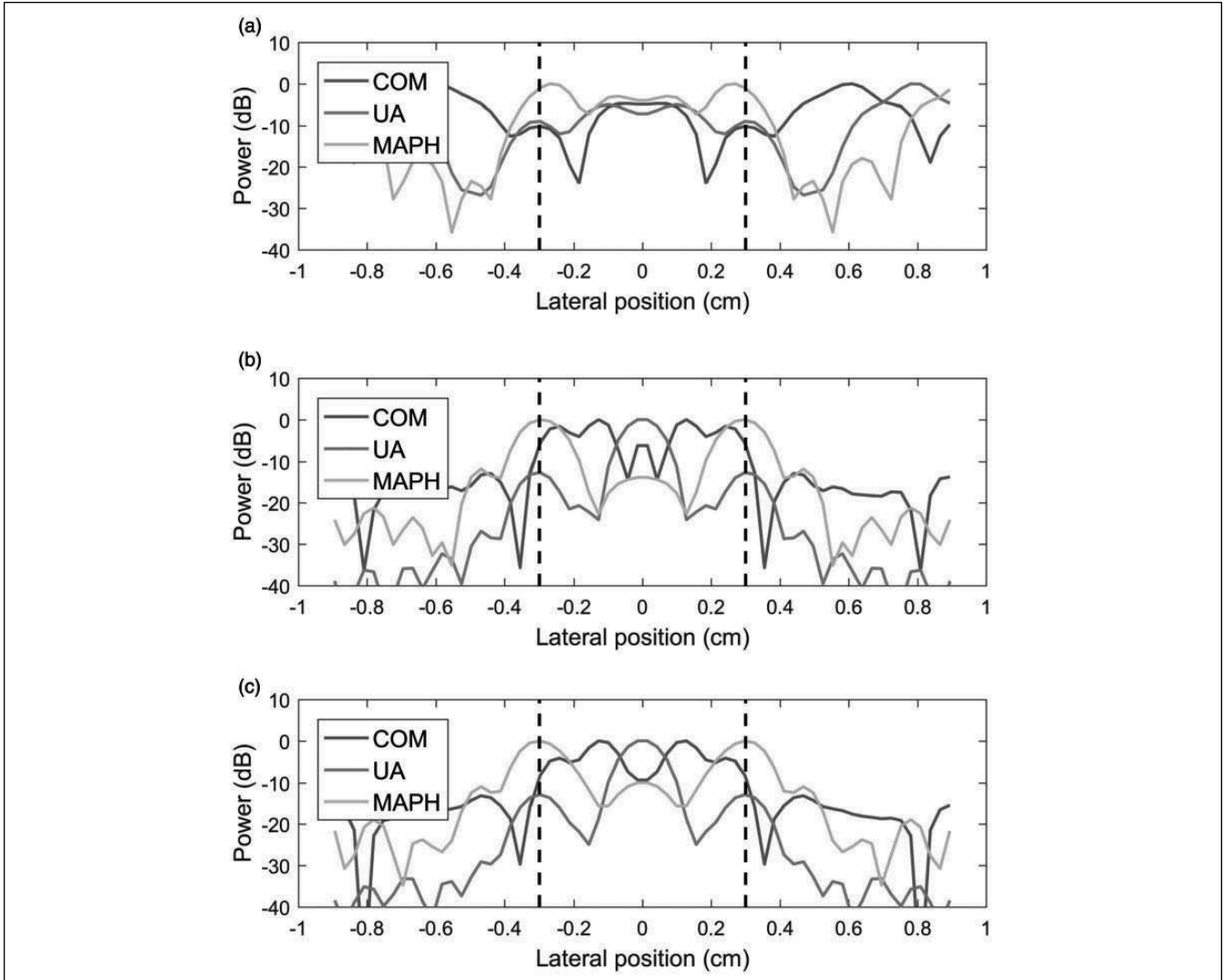
Figure 11. The effect of impedance contrast on B-mode images of smooth, hard inclusions; the variation of power along a line in the lateral direction through the inclusion, $P_k(z_* = 2.3\text{cm})$, for incompressible and compressible elastic inclusions with identical impedance contrast are shown in (a) and (b), respectively. The variation of power along the line for compressible elastic inclusion in viscoelastic host is shown in (c). Three different types of stones are compared, calcium oxalate (COM), uric acid (UA), and magnesium ammonium phosphate hexahydrate (MAPH). The dashed lines denote the extremities of the inclusion in all plots.

artifacts in the images are exacerbated by the surface roughness of the compressible elastic inclusion.

Effect of host–inclusion impedance contrast. We plot the variation of power along axial and lateral directions in the B-mode image (Equation (14)) for inclusions with varying impedance contrast to study its effect on reverberation-induced backscatter. The variation of power along the thirty second A-line for the incompressible and compressible elastic inclusions embedded in an incompressible elastic host for three different impedance contrasts are shown in Figure 10(a) and (b), respectively. Figure 10(c) shows the power variation in the axial direction for a compressible elastic inclusion in viscoelastic host tissue. Two prominent peaks are seen in the incompressible

elastic case, whereas a steady reduction of power is observed in compressible elastic inclusion cases. In Figure 10, the brightest pixel in the B-mode image is used as the normalization constant for computing the power (i.e., $BM_z^{\text{ref}} = BM_{32}(z \approx 2.1\text{cm})$ in Equation (14)). Thus, the spread of brightness behind the inclusion for different material models can be compared by observing the difference in the power at $z \approx 2.1$ cm and $z \approx 3.3$ cm. A careful observation of Figure 10(a) shows that the power at $z \approx 3.3$ cm is of the order of -60 dB for the incompressible elastic inclusion. In Figure 10(b) and (c), the power at $z \approx 3.3$ cm is of the order of -35 dB. The spread of brightness behind the stone is, thus, significantly lower for the incompressible elastic inclusion, as compared with the compressible elastic inclusion. Notice that a change in
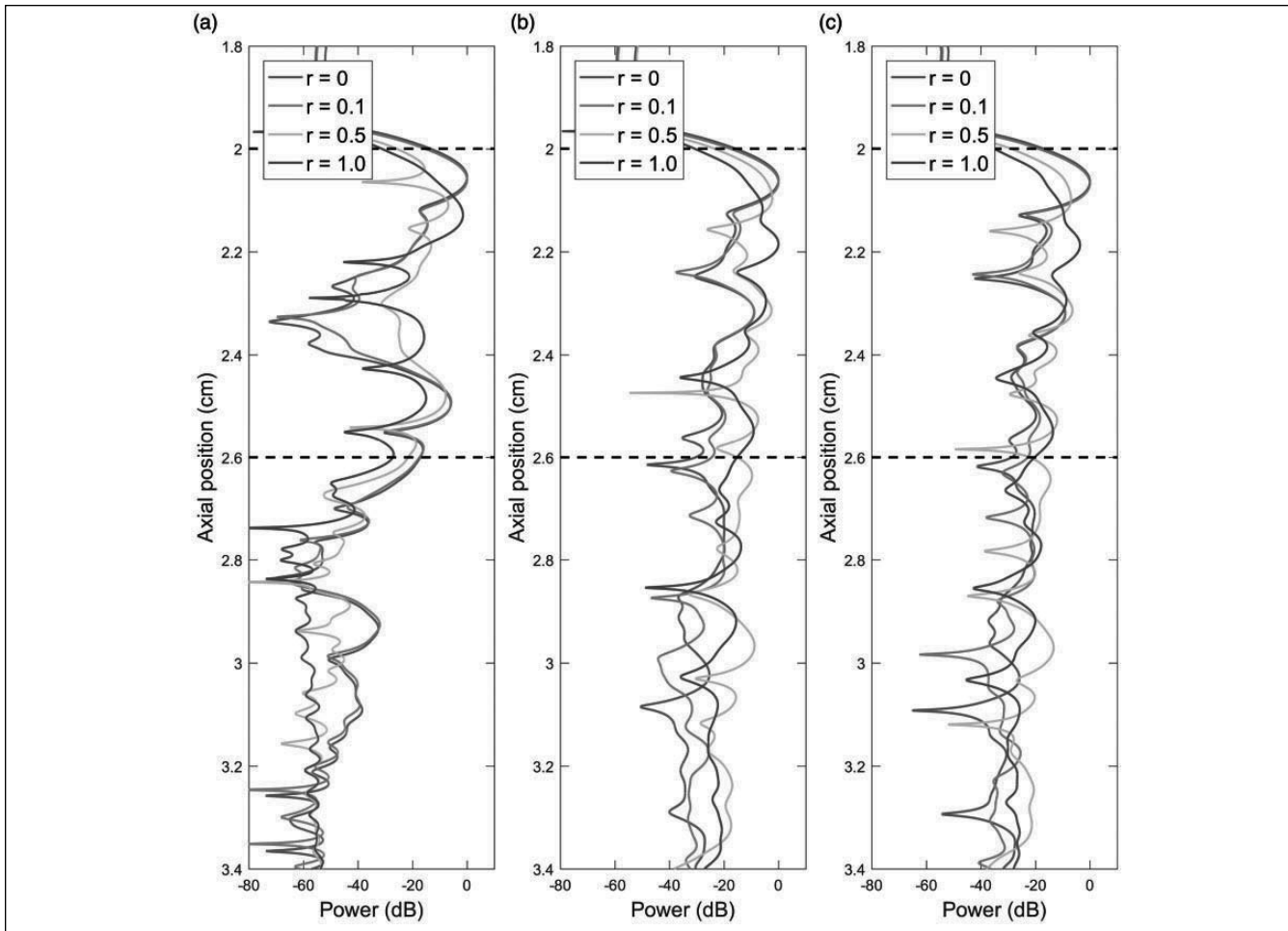
Figure 12. The effect of surface roughness on B-mode images of hard inclusions; the variation of power ($P_{32}(z)$ in Equation (14)) through the depth for incompressible and compressible elastic inclusions with identical impedance contrast are shown in (a) and (b), respectively. The variation of power along the depth for compressible elastic inclusion in viscoelastic host is shown in (c). Three different types of stones are compared, calcium oxalate (COM), uric acid (UA), and magnesium ammonium phosphate hexahydrate (MAPH). The dashed lines denote the extremities of the inclusion in all plots.

impedance contrast does not change the general trend in the decay of brightness behind the inclusion for the different material models used in our simulations. Also, it seems that the attenuation in the viscoelastic tissue does not significantly affect the relative brightness (power) along the axial direction.

The variations of power along a line in the lateral direction through the inclusion for the incompressible and compressible elastic inclusions in incompressible elastic host are shown in Figure 11(a) and (b), and the same for an compressible elastic inclusion in a viscoelastic host medium is shown in Figure 11(c). We notice that the assumption of stone incompressibility affects the spread of brightness in the lateral direction. For the incompressible elastic inclusion, the power at the lateral extremities of the inclusion is about –35 dB in Figure 11 (a), whereas that for the case of the compressible inclusion is about only –20 dB in Figure 11(b) and (c). This

suggests that for incompressible (acoustic) inclusions, the decrease in the power or brightness (to a certain dB value) may indicate the extremities of the inclusion, whereas the same procedure may lead to erroneous size estimation in the case of an elastic inclusion.

The effect of inclusion roughness. The effect of surface roughness on B-mode images is shown in Figure 12. It can be seen in Figure 12(a), (b), and (c) that the prominent leading peak in the B-mode image (observed near $z = 2.0$ cm for $r = 0$ case) moves downward as the roughness parameter (r) value increases. For a rough inclusion, the location of the top boundary of the central core of the inclusion moves away from the transducer, as the r value increases (center of the inclusion and outer radius of the inclusion R_{out} remain constant across all r values). Therefore, the second peak in the B-mode image moves axially away from the transducer. Furthermore,
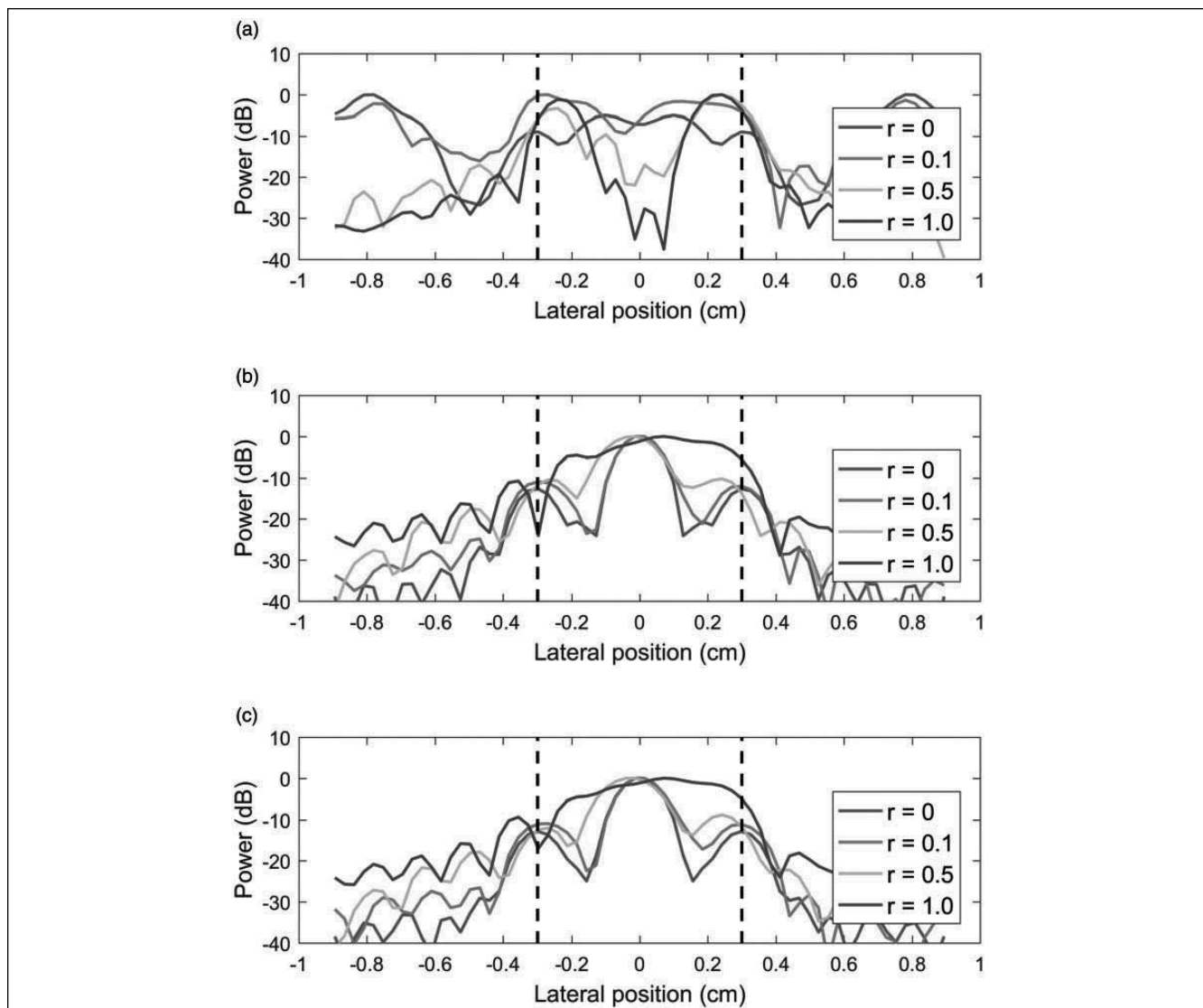
Figure 13. The effect of surface roughness on B-mode images of hard inclusions; the variation of power along a line in the lateral direction through the inclusion, $P_k(z_* = 2.3\text{cm})$, for incompressible and compressible elastic inclusions with identical impedance contrast are shown in (a) and (b), respectively. The variation of power in the lateral direction for compressible elastic inclusion in viscoelastic host is shown in (c). Three different types of stones are compared, calcium oxalate (COM), uric acid (UA), and magnesium ammonium phosphate hexahydrate (MAPH). The dashed lines denote the extremities of the inclusion in all plots.

there is an increase in the power behind the stone for rough inclusions. Figure 13(a), (b), and (c) shows that the reduction in power along the lateral direction (as one moves away from the center of the inclusion) occurs to a lesser extent in the case of rough inclusions. Also, we find that the decrease in brightness near the along the host–inclusion boundary in the lateral direction for the rough incompressible inclusion (Figure 13a) is lesser than that for the smooth incompressible inclusion (Figure 11a). A similar trend is seen for the case of the rough elastic inclusions, although the spread of brightness in the lateral direction is exacerbated by the surface roughness (Figure 13b and c). This study suggests that surface roughness affects lateral power variation, thus

causing a significant challenge for the estimation of size of the inclusion.

Conclusion

In this article, we performed finite element simulations of wave scattering in the soft-tissue environment with embedded stones or metal objects by idealizing it as a (host–inclusion) material medium with different constitutive behaviors. The goal of this work was to demonstrate the effect of constitutive behavior and surface roughness on reverberation-induced backscatter and the spread of brightness observed in B-mode images of stones embedded in soft tissue. We excited the medium

with near-plane waves emitted by a transducer by prescribing suitable boundary conditions on the top surface of the host domain. We then collected the scattered wave response at the transducer boundary from the simulation results and used it to form B-mode images. The novelty of our study is that we analyzed brightness characteristics of B-mode images using a compressible linear elastic constitutive model for the stone, instead of a linear acoustic model, which allows for the propagation of both pressure and shear waves within the stone due to mode conversion at the stone–tissue interface. We also studied the effect of time-dependent deformation response of the tissue by defining viscoelastic material model parameters that mimic wave attenuation in soft tissues. We verified the linear model behavior of our finite element simulation framework by comparing the PSF results (i.e., B-mode images) from simulations with those from the Field II program. We also validated the simulation framework by comparing the images of rough and smooth surfaced circular inclusions with experimental images of a cylindrical metal tool immersed in a water tank.

Characteristic features of brightness observed behind the inclusion may be used to detect the presence of a hard inclusion (e.g., kidney stone), but the spread of brightness in the lateral direction around the inclusion could introduce an error in inclusion size estimation. To gain a better understanding of the mechanisms behind brightness characteristics in B-mode images of hard inclusions embedded in soft tissues, we performed simulation studies with circular inclusions by varying the compressibility of the elastic inclusion, impedance contrast between the host and inclusion, and the surface roughness of the inclusion. Our simulation studies provided several useful insights:

1. The reverberation of shear waves inside the inclusion is a key phenomenon responsible for the backscatter observed in B-mode images of hard elastic inclusions embedded in soft tissues; this behavior is in agreement with theoretical and analytical investigations reported in the literature.
2. A viscoelastic tissue model with attenuation similar to that typically assumed in acoustic wave simulators (0.7 dB/cm/MHz) shows brightness characteristics similar to an elastic tissue model without much attenuation (for the inclusion depths considered in this study); this conclusion could benefit future modelers by allowing them to simplify the tissue model and reduce the computational burden.
3. The spread of brightness behind the inclusion, seen in B-mode images, cannot be simulated using acoustic material model with high impedance contrast with the background tissue; this implies that simulation-based studies aimed at investigating the utility of

reverberation artifact for performing hard inclusion sizing should consider an elastic material model for the inclusion.
4. The surface roughness of the inclusion exacerbates the spread of brightness both in axial and lateral directions in a B-mode image; this phenomenon explains (at least, in part) the difficulty in inclusion size estimation using B-mode imaging.

These observations and insights will inform future simulation studies addressing the kidney stone imaging problem. We also acknowledge the limitations of the current study and discuss the specifics of future work. A major limitation of this study is that we only considered near-plane wave transmissions from the transducer, which is a contemporary approach to ultrasonic pulse sequence. Currently, due to computational limitations, we chose to investigate only near-plane wave transmissions. The periodic stone surface roughness model used in this work is not observed in real hard inclusions, such as kidney stones, which is another limitation of this study. In future, we will consider focused and multi-angled plane wave transmissions with synthetic transmit imaging and incorporate realistic stone geometries[46] characterized using advanced tomography or microscopy techniques. In this work, our stone-like inclusions produced bright tails, but in reality, stones usually exhibit shadows rather than bright trailing tails. The presence of a shadow can be partly explained by a brighter background region than the one used in our simulation studies. However, another major limitation is that we considered fundamental B-mode imaging, instead of the commonly used harmonic imaging. The wave physics models used here can be extended to include nonlinear effects, and in turn, enable harmonic mode imaging. In future, we will investigate (second) harmonic B-mode imaging of rough, hard inclusions embedded in soft tissues to better understand the role of nonlinear effects in producing the shadow artifact.[47]

Declaration of Conflicting Interests

Funding

ORCID iDs

Pranav M. Karve ⓘ https://orcid.org/0000-0002-4363-5255
Kazuyuki Dei ⓘ https://orcid.org/0000-0002-9174-2645

References

1. Ulusan S, Koc Z, Tokmak N. Accuracy of sonography for detecting renal stone: comparison with CT. J Clin Ultrasound. 2007;35(5):256–61. doi:10.1002/jcu.20347.

2. Huang J, Triedman JK, Vasilyev NV, Suematsu Y, Cleveland RO, Dupont PE. Imaging artifacts of medical instruments in ultrasound-guided interventions. J Ultrasound Med. 2007;26(10):1303–22. doi:10.7863/jum.2007.26.10.1303.

3. Fowler KAB, Locken JA, Duchesne JH, Williamson MR. US for detecting renal calculi with nonenhanced CT as a reference standard. Radiology. 2002;222(1):109–113. doi:10.1148/radiol.2221010453.

4. Unal D, Yeni E, Karaoglanoglu M, Verit A, Karatas OF. Can conventional examinations contribute to the diagnostic power of unenhanced helical computed tomography in urolithiasis? Urol Int. 2003;70(1):31–5.

5. Ray AA, Ghiculete D, Pace KT, D'A Honey RJ. Limitations to ultrasound in the detection and measurement of urinary tract calculi. Urology. 2010;76(2):295–300. doi:10.1016/j.urology.2009.12.015.

6. Kanno T, Kubota M, Sakamoto H, Nishiyama R, Okada T, Higashi Y, et al. The efficacy of ultrasonography for the detection of renal stone. Urology. 2014;84(2):285–88. doi:10.1016/j.urology.2014.04.010.

7. Ganesan V, De S, Greene D, Torricelli FC, Monga M. Accuracy of ultrasonography for renal stone detection and size determination: is it good enough for management decisions. BJU Int. 2017;119(3):464–69. doi:10.1111/bju.13605.

8. Kremkau FW, Taylor KJ. Artifacts in ultrasound imaging. J Ultrasound Med. 1986;5(4):227–37. doi:10.7863/jum.1986.5.4.227.

9. Scanlan KA. Sonographic artifacts and their origins. AJR Am J Roentgenol. 1991;156(6):1267–72. doi:10.2214/ajr.156.6.2028876.

10. Hefner LV, Goldstein A. Resonance by rod-shaped reflectors in ultrasound test objects. Radiology. 1981;139(1):189–93. doi:10.1148/radiology.139.1.7208920.

11. Wendell BA, Athey PA. Ultrasonic appearance of metallic foreign bodies in parenchymal organs. J Clin Ultrasound. 1981;9(3):133–35. doi:10.1002/jcu.1870090307.

12. Shapiro RS, Winsberg F. Comet-tail artifact from cholesterol crystals: observations in the postlithotripsy gallbladder and an in vitro model. Radiology. 1990;177(1):153–56. doi:10.1148/radiology.177.1.2204960.

13. Lichtenstein D, Maziare G, Biderman P, Gepner A, Barré O. The comet-tail artifact. Am J Respir Crit Care Med. 1997;156(5):1640–46. doi:10.1164/ajrccm.156.5.96-07096.

14. Lim JH, Lee KS, Kim TS, Chung MP. Ring-down artifacts posterior to the right hemidiaphragm on abdominal sonography: sign of pulmonary parenchymal abnormalities. J Ultrasound Med. 1999;18(6):403–10. doi:10.7863/jum.1999.18.6.403.

15. Laing FC, Kurtz AB. The importance of ultrasonic sidelobe artifacts. Radiology. 1982;145(3):763–68. doi:10.1148/radiology.145.3.7146410.

16. Abbott JG, Thurstone FL. Acoustic speckle: theory and experimental analysis. Ultrason Imaging. 1979;1(4):303–24. doi:10.1016/0161-7346(79)90024-5.

17. Wells P, Halliwell M. Speckle in ultrasonic imaging. Ultrasonics. 1981;19(5):225–29. doi:10.1016/0041-624X(81)90007-X.

18. Sommer FG, Filly RA, Minton MJ. Acoustic shadowing due to refractive and reflective effects. Am J Roentgenol. 1979;132(6):973–79.

19. Zdero R, Fenton P, Bryant JT. Diagnostic ultrasound artifacts during imaging of two-body interfaces: Part 1—wavelength resonance. Ultrasonics. 2002;39(10):681–88. doi:10.1016/S0041-624X(02)00381-5.

20. Feldman MK, Katyal S, Blackwood MS. US artifacts. RadioGraphics. 2009;29(4):1179–89. doi:10.1148/rg.294085199.

21. Hindi A, Peterson C, Barr R. Artifacts in diagnostic ultrasound. Rep Med Imag. 2013;2013(1):29–48. Available from https://www.ingentaconnect.com/content/doaj/11791586/2013/00002013/00000001/art00002.

22. Faran JJ, Jr. Sound scattering by solid cylinders and spheres. J Acoust Soc Am. 1951;23(4):405–18. doi:10.1121/1.1906780.

23. Hickling R. Analysis of echoes from a solid elastic sphere in water. J Acoust Soc Am. 1962;34(10):1582–92. doi:10.1121/1.1909055.

24. Neubauer WG, Dragonette LR. Observation of waves radiated from circular cylinders caused by an incident pulse. J Acoust Soc Am. 1970;48(5B):1135–49 doi:10.1121/1.1912254.

25. Schuetz LS, Neubauer WG. Acoustic reflection from cylinders—nonabsorbing and absorbing. J Acoust Soc Am. 1977;62(3):513–17. doi:10.1121/1. 381569.

26. Flax L, Varadan VK, Varadan VV. Scattering of an obliquely incident acoustic wave by an infinite cylinder. J Acoust Soc Am. 1980;68(6):1832–35. doi:10.1121/1.385173.

27. Fan Y, Honarvar F, Sinclair AN, Jafari MR. Circumferential resonance modes of solid elastic cylinders excited by obliquely incident acoustic waves. J Acoust Soc Am. 2003;113(1):102–13. doi:10.1121/1.1525289.

28. Zarse CA, Hameed TA, Jackson ME, Pishchalnikov YA, Lingeman JE, McAteer JA, et al. CT visible internal stone structure, but not Hounsfield unit value, of calcium oxalate monohydrate (COM) calculi predicts lithotripsy fragility in vitro. Urol Res. 2007;35(4):201–206. doi:10.1007/s00240-007-0104.

29. Bhatta KM, Prien EL Jr, Dretler SP. Cystine calculi—rough and smooth: a new clinical distinction. J Urol. 1989;142(4):937–40. doi:10.1016/S0022-5347(17)38946-2.

30. Jensen JA, Svendsen NB. Calculation of pressure fields from arbitrarily shaped, apodized, and excited ultrasound transducers. IEEE Trans Ultrason Ferroelectrics Freq Contr. 1992;39(2):262–67. doi:10.1109/58.139123.

31. Jensen JA. Field: a program for simulating ultrasound systems. In: Proceedings of the 10th Nordic-Baltic Conference

on Biomedical Imaging Published in Medical & Biological Engineering & Computing, pp. 351-53.

32. McGough RJ, Samulski T, Kelly J. An efficient grid sectoring method for calculations of the near-field pressure generated by a circular piston. J Acoust Soc Am. 2004;115(5):1942–54.

33. Pinton GF, Dahl J, Rosenzweig S, Trahey GE. A heterogeneous nonlinear attenuating full-wave model of ultrasound. IEEE Trans Ultrason Ferroelectr Freq Control. 2009;56(3):474–88. doi:10.1109/TUFFC.2009.1066.

34. Treeby BE, Cox BT. k-wave: MATLAB toolbox for the simulation and reconstruction of photoacoustic wave fields. J Biomed Optic. 2010;15(2):021314. doi:10.1117/1.3360308.

35. Kremkau FW. Physical principles of ultrasound. Semin Roentgenol. 1975;10(4):259–263.

36. Hangiandreou NJ. AAPM/RSNA physics tutorial for residents: topics in US. RadioGraphics. 2003;23(4):1019–33.

37. Bathe K. Finite Element Procedures. Englewood Cliffs, New Jersey: Prentice-Hall, Inc.; 2006.

38. Dahake G, Gracewski SM. Finite difference predictions of P-SV wave propagation inside submerged solids. I. Liquid–solid interface conditions. J Acoust Soc Am. 1997;102(4):2125–37. doi:10.1121/1.419592.

39. Dahake G, Gracewski SM. Finite difference predictions of P-SV wave propagation inside submerged solids. II. Effect of geometry. J Acoust Soc Am. 1997;102(4):2138–45. doi:10.1121/1.419593.

40. Mihradi S, Homma H, Kanto Y. Numerical analysis of kidney stone fragmentation by short pulse impingement.

41. Cleveland RO, Sapozhnikov OA. Modeling elastic wave propagation in kidney stones with application to shock wave lithotripsy. J Acoust Soc Am. 2005;118(4):2667–76. doi:10.1121/1.2032187.

42. Zhong P, Chuong CJ, Preminger GM. Characterization of fracture toughness of renal calculi using a microindentation technique. J Mater Sci Lett. 1993;12(18):1460–62. doi:10.1007/BF00591608.

43. Culjat MO, Goldenberg D, Tewari P, Singh RS. A review of tissue substitutes for ultrasound imaging. Ultrasound Med Biol. 2010;36(6):861–73. doi:10.1016/j.ultrasmedbio.2010.02.012.

44. DeGarmo EP, Black JT, Kohser RA. Materials and Processes in Manufacturing. Chichester: John Wiley & Sons Ltd.; 2003.

45. *ABAQUS 6.13 Documentation*. Providence, RI: Dassault Systémes; 2013.

46. Duan X, Qu M, Wang J, Trevathan J, Vrtiska T, Williams JC, Jr., et al. Differentiation of calcium oxalate monohydrate and calcium oxalate dihydrate stones using quantitative morphological information from micro-computerized and clinical computerized tomography. J Urol. 2013;189(6):2350–56. doi:10.1016/j.juro.2012.11.004.

47. Dunmire B, Harper JD, Cunitz BW, Lee FC, Hsi R, Liu Z, et al. Use of the acoustic shadow width to determine kidney stone size with ultrasound. J Urol. 2016;195(1):171–77. doi:10.1016/j.juro.2015.05.111.

JSME Int J A-Solid M. 2004;47(4):581–90. doi:10.1299/jsmea.47.581.